

Microseismic Monitoring of a Controlled Collapse in Field II at Ocnele Mari, Romania

C-I. TRIFU¹ and V. SHUMILA¹

Abstract—Several decades of faulty exploitation of salt through solution mining led to the creation of an underground cavern containing several million cubic meters of brine. To eliminate the huge hazard near a densely inhabited area, a technical solution was implemented to resolve this instability concern through the controlled collapse of the roof while pumping the brine out and filling the cavern with sterile. To supervise this, an area of over 1 km² was monitored with a staggered array of 36 one-component, 15 Hz geophones installed in 12 boreholes about 160–360 m deep. A total of 2,392 seismic events with M_w –2.6 to 0.2 occurred from July 2005 to March 2006, located within an average accuracy of 18 m. The b -value of the frequency-magnitude distribution exhibited a time variation from 0.5 to 1 and from there to 1.5, suggesting that the collapse initiated as a linear fracture pattern, followed by shear planar fragmentations and finally a 3-D failure process. The branching ratio of seismicity is indicative of a super-critical process, except for a short period in mid-February when temporary stability existed. Event relocation through the use of a collapsing technique outlines that major clusters of seismicity were associated with the main cavern collapse, whereas smaller clusters were generated by the fracturing of smaller size nearby caverns. It is shown that one-component recordings allow for stable and reliable point source event mechanism solutions through automatic moment tensor inversion using time domain estimates of low frequency amplitudes with first polarities attached. Detailed analysis of failure mechanism components uses 912 solutions with conditional number $CN < 100$ and a correlation coefficient $r^2 > 0.5$. The largest pure shear (DC) components characterize the events surrounding the cavern ceiling, which exhibit normal and strike-slip failures. The majority of mechanism solutions include up to 30% explosional failure components, which correspond to roof caving under gravitational collapsing. The largest vertical deformation rate relates closely to the cavern roof and floor, as well as the rest of the salt formation, whereas the horizontal deformation rate is most prominent in areas of detected collapses.

1. Introduction

The salt deposit of Ocnele Mari is located in the sub-Carpathian hills of southern Romania. About 8 km long, it runs from east to west, with a width of 3.5 km and a thickness of up to 400 m, dipping about 20° to the north (Fig. 1). Salt has been exploited through dissolution in four fields which entered in production sequentially, beginning with 1954. Operations in Field II were initiated in 1969 and led to the extraction of 13.5 million tones of salt until a major collapse occurred in March 1991. This event underscored the risks associated with the presence of large dissolution chambers close to a densely populated area, prompting the decision to shut-down the field (ZAMFIRESCU *et al.* 2007a).

Cavernometry measurements carried out in 1993 outlined the presence of a massive cavern formed by the complete dissolution of the inter-chamber pillars of 6 of the 15 wells, containing 5.5 million m³ of compressed brine. Another major collapse took place towards the northern edge of the cavern in September 2001, when a part of the roof caved in, forming a quasi-circular crater of almost 200 m in diameter and leading to the spill of 1.7 million m³ of brine. The ground material plunged from the surface, however, acted like a cork, stopping a larger outflow of brine. A second major event occurred in July 2004, during which the original sinkhole was enlarged, accelerating thus the demand for a solution to this mechanical instability problem.

A description detailing how the controlled collapse of the cavern roof was designed and carried out is presented by ZAMFIRESCU *et al.* (2007b). In short, a fragmentation process was sought by cutting open a part of the cavern roof, pumping the brine out and

¹ Engineering Seismology Group Inc., Kingston, ON K7K 7G3, Canada. E-mail: trifu@esg.ca

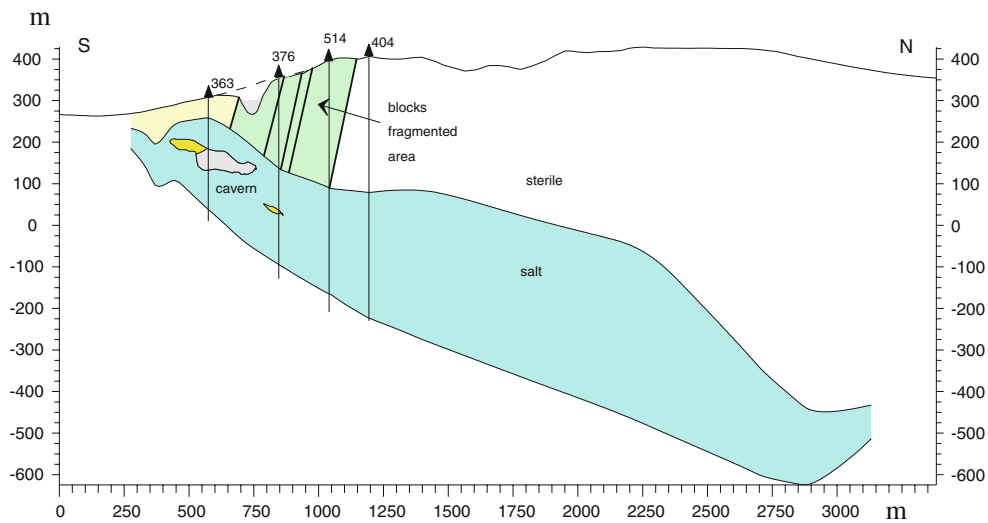


Figure 1
Cross-section of the Ocnele Mari salt formation

introducing sterile in the cavern all simultaneously to keep overall hydraulic pressure stable. A subsurface seismic array consisting of one-component geophones was installed around the cavern to continuously monitor an area of about 1 km² to ensure the safety of the workforce and equipment employed, as well as to offer quantitative information about the stress redistribution, indicative as to how the collapse proceeded.

It is for the first time that passive microseismic technology is used for the monitoring of a controlled roof collapse in a solution mine field. This study documents the seismic array design and undertakes an analysis of the seismic data recorded between July 2005 and March 2006. The mechanisms of the seismic events induced during the controlled collapse are subsequently investigated using the seismic moment tensor inversion from one-component recordings. The reliability of such inversions is analyzed for the sensor array employed, after which the spatial distribution of different failure components is examined. Based on the derived mechanism solutions, an estimate of the seismic deformation field is finally obtained.

In addition to the microseismic array, topographic marks were installed to provide settlement data. Various other geotechnical measurements were regularly carried out during the controlled collapse, such as surface crack orientation and size, rate of water

inflow, brine pressure, etc. The study of the relationship between changes in these parameters and microseismicity will be the subject of a future analysis.

2. Microseismic Array

A monitoring system was specifically designed to identify, locate and report in real-time on the occurrence of microseismic activity as a result of stress redistribution during various stages of the controlled collapse. The system included a staggered array of 36 sensors installed in 12 boreholes, three sensors per hole (Fig. 2). Sensors are one-component, omnidirectional 15 Hz geophones with a sensitivity of 43.3 V/m/s, in stainless steel cases with polyurethane jacket cables to withstand the very corrosive medium. The boreholes were drilled vertically and were cased to avoid accidental closure. Each three-unit geophone string was installed attached to a support pipe and grouted in place by pouring the cement through this pipe directly to the bottom of the hole to ensure a tight, airless grouting.

The array geometry was designed to provide an average event location accuracy of 20–30 m throughout the entire monitoring volume, while being capable of identifying events with magnitudes as low as -1.5 . As such, the boreholes were rather evenly

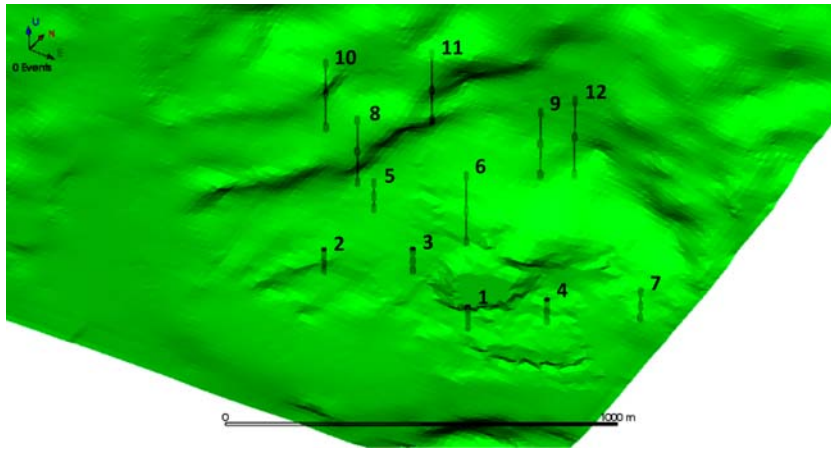


Figure 2
Array geometry; numbers correspond to boreholes and scale bar is 1,000 m

spaced at approximately 200 m, avoiding though any placement too close to the sinkhole. The depth of each hole was designed to ensure that the bottom sensor is located within the salt layer, thus reaching at times close to 400 m below surface.

A 24-bit Paladin seismic recorder manufactured by Engineering Seismology Group was placed on top of each hole, along with external amplifiers, lightning protection, power supply and 2.4 GHz radio Ethernet communication. Paladin is a web-enabled device

capable of operating simultaneously in a continuous and triggered mode at up to 20 kHz sampling frequency with an effective dynamic range of 120 dB. For this application, data sampling was carried out at 2 kHz. GPS units employed for time synchronization offered a better than 1 μ s accuracy. Radio signals were collected at a central control station either directly or through up to two repeaters, depending on the local topography. Example waveforms are shown in Fig. 3.

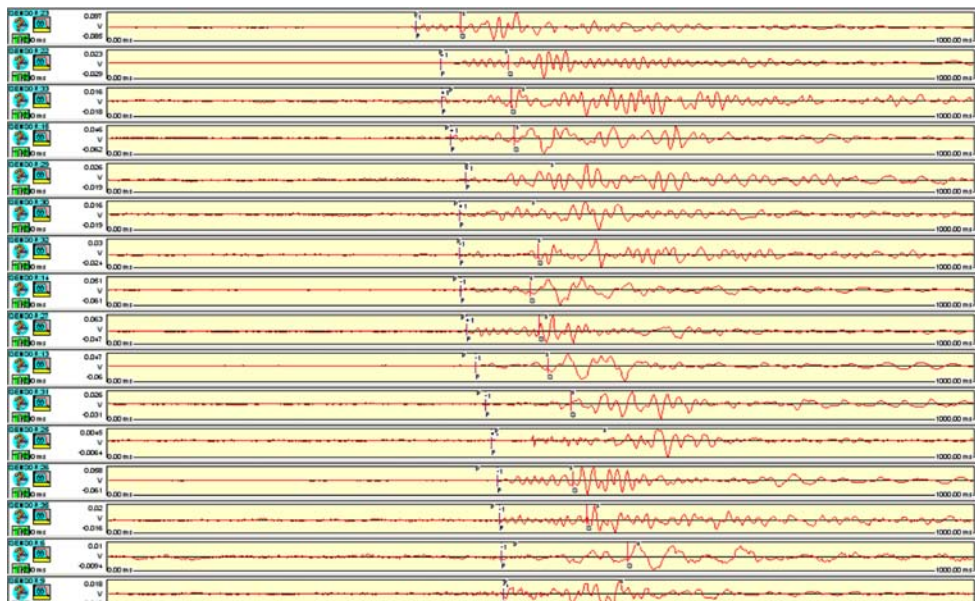


Figure 3
Example waveforms recorded for a seismic event which occurred at Ocele Mari

3. Seismic Data, Location of Seismicity and Seismic Regime

Constant P- and S-wave velocities were initially estimated from calibration blasts and used to calculate event locations. Stations with time residuals in excess of 20 ms were filtered out. Figure 4 shows the difference between any combination of source-receiver straight raypaths for each actual event and the time difference between associated wave arrivals. The results indicate $V_P = 2933 \pm 11$ m/s and $V_S = 1,700 \pm 8$ m/s. This procedure was preferred to the direct absolute distance versus time plot, because it is independent from the origin times and increases the statistics.

A total of 2,392 events were recorded between July 7, 2005 and March 11, 2006. Seismic activity

included three outburst episodes associated with two minor collapses in October and November, and the major cavern collapse at the end of December. Event locations employed first P-wave arrivals at 5 to 31 sensors (most often 8 to 13) and S-wave arrivals at $\frac{1}{4}$ to $\frac{1}{2}$ that many in a Simplex algorithm with L1 norm minimization of time residuals (PRESS *et al.* 1989). Only 7% of event locations did not use S-wave arrivals. Total location errors (square root of the sum of squared location coordinate errors) fit closely a normal distribution with a mean of 18 m and a standard deviation of 8 m (Fig. 5).

Moment magnitudes are between -2.6 and 0.2 . Frequency-magnitude distribution exhibits a linear trend between $M_w - 1.5$ and -0.3 with a b -value of 1.5 (Fig. 6). The distribution of event locations is presented in Fig. 7a along with local structures. The top

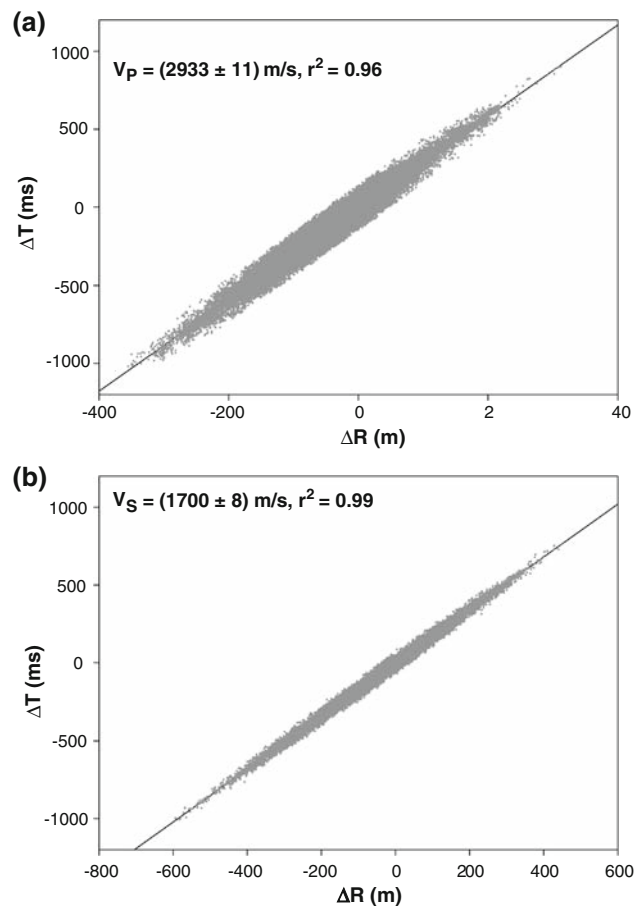


Figure 4
P- (a) and S-wave (b) velocity estimates

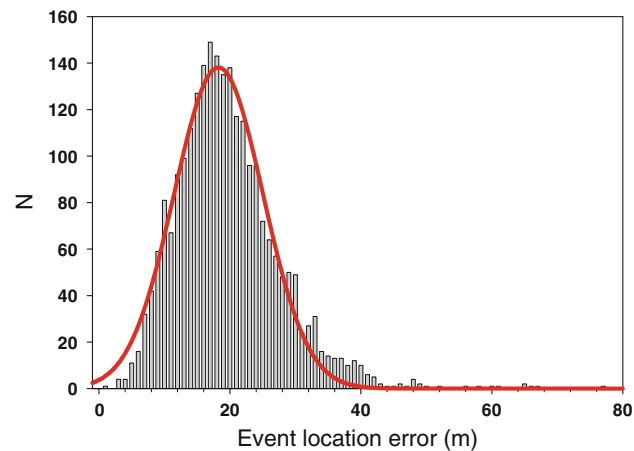


Figure 5

Distribution of event location errors; the curve corresponds to a normal distribution with a mean of 18 m and a standard deviation of 8 m

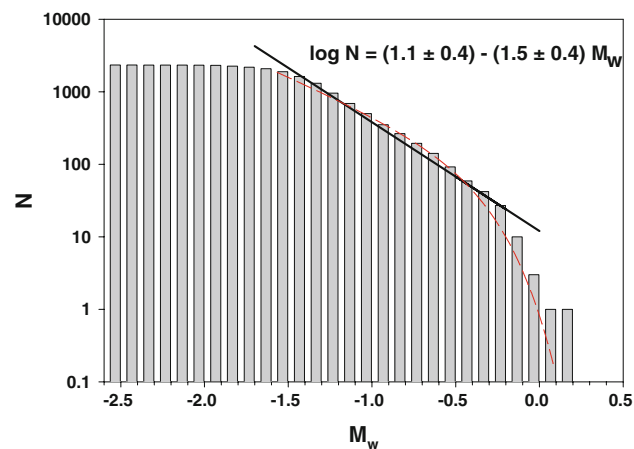


Figure 6

Cumulative frequency-magnitude distribution

surface corresponds to the local topography, whereas the lower surfaces correlate to the roof and the floor of the original large underground salt cavern. Most of the seismicity induced by the controlled collapse appears to be indeed related to the fragmentation and falling of the roof. Deeper seismicity located in the cavern was likely caused by subsequent nearby falling debris during strata readjustment to a new equilibrium.

Uncertainties in wave velocity and misidentification of first wave arrivals due to low signal-to-noise ratios contributed to increased location errors, thus leading to a blurry picture. Assuming that event locations should be better related to local structures and active processes take place in the field, an attempt was made to improve the relative event

location accuracy by employing a collapsing technique (JONES and STEWART 1997). This technique considers that event location errors are normally distributed and the event position within the corresponding ellipsoid of uncertainty is random. As such, each event location could be moved within its ellipsoid of uncertainty towards a location that is consistent with locations of other events that fall inside the same ellipsoid. The algorithm optimizes the overall consistency of relocated events with the original event location uncertainties.

The results are presented in Fig. 7b–d and several general characteristics are instantly apparent. The distribution of seismicity is composed of several spatially tight clusters. Most active clusters are

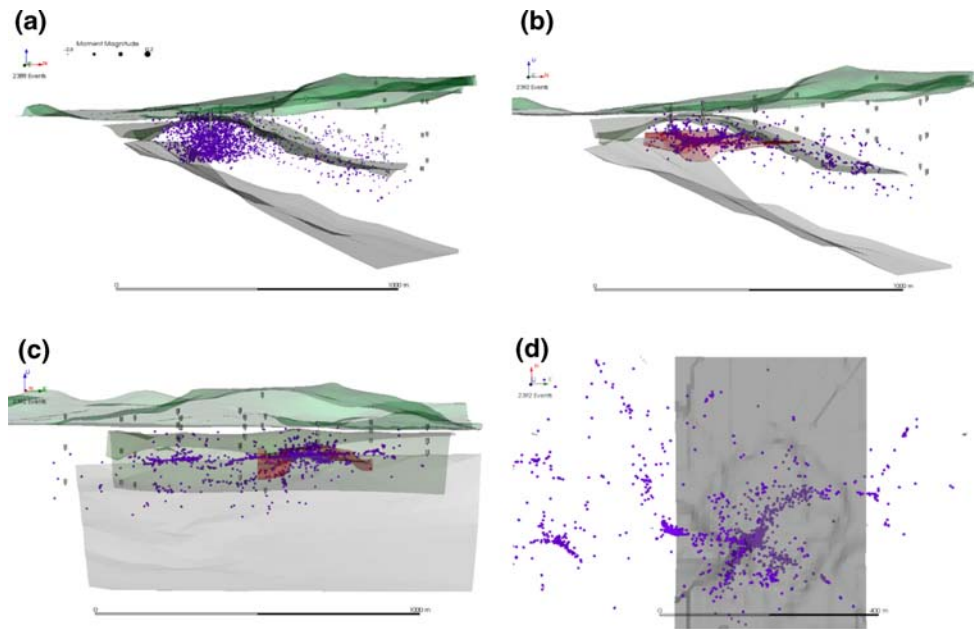


Figure 7

Absolute (a) and relative event locations (b–d) in vertical cross-section striking north (a–b), east (c) –scale bar 1,000 m, and in north-east plan view –scale bar 400 m (d)

located in the central-southern part of the monitoring region and exhibit a remarkable correlation with the cavern ceiling surveyed in 2002. This observation strongly supports the conclusion that the larger part of the induced microseismicity is a direct result of the major cavern collapse. Smaller and less active clusters of seismicity are likely related to roof fragmentations of smaller, nearby caverns. These results offer increased confidence in the fact that seismic data contain relevant information for the understanding of the geotechnical processes that took place during the controlled collapse.

In the framework of the Epidemic Type Earthquake Sequence, the average number of off-springs generated by each event is defined as the branching ratio (HELMSTETTER and SORNETTE 2002). Figure 8 shows the time variation of the b -value and branching ratio using a 2-week moving window with a step of 24 h. The b -value is close to 0.5 from July to September 2005, increases and varies around 1 until January 2006, after which it drops slightly in February and then increases to approximately 1.5 in March 2006. The branching ratio consists of values that define a super-critical seismic regime (>1) over the entire period of time in this analysis, except for the mid-February 2006, when the

off-springs died out and seismic regime became stable (<1). This is in striking contrast for example with the behavior of mine induced seismicity, which commonly appears to be a stable regime and only rarely super-critical (TRIFU and SHUMILA 2005).

The variations in the b -value from 0.5 to 1 and then to 1.5 seem to indicate changes in the general pattern of the fracture process within the monitoring volume. It suggests that the fracture process initiated as a linear fracture pattern ($D = 2b = 1$). Three months later roof fragmentation was well developed and shear fractures dominated ($D = 2$), while towards the end of the reported period fractures occurred within the entire volume ($D = 3$). The branching ratios indicate that once the roof fragmentation process began, the fracturing continued super-critically. Worth noting, it persisted for about another month after the large roof collapse at the end of December 2005.

4. Stability and Reliability of Seismic Moment Tensor Inversions

The use of one-component recordings maintains the linear dependence of the low frequency far-field

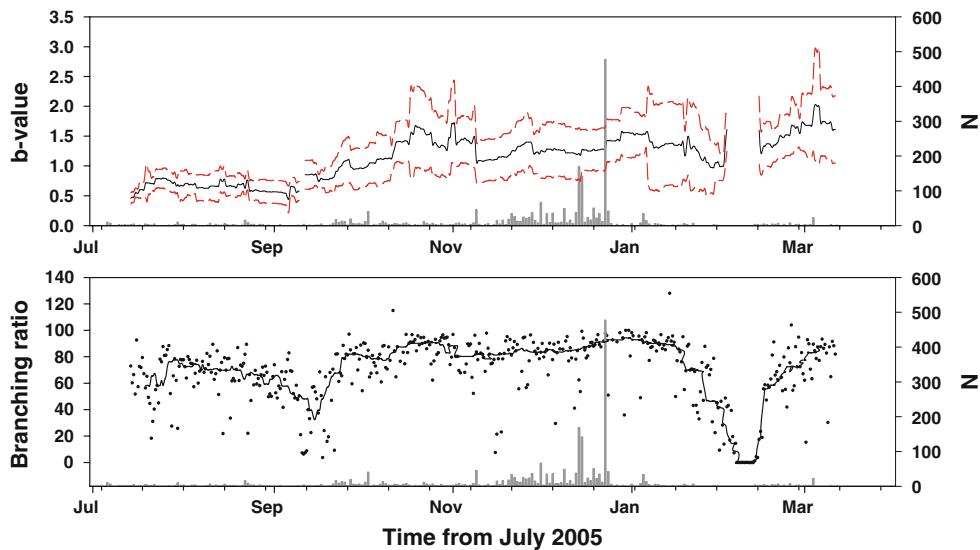


Figure 8

Time variation of the b -value (a) and branching ratio (b). Dashed lines in (a) denote the standard deviation and continuous line in (b) represents median estimates

displacements, with first polarities included, on the six unknown components of the symmetrical seismic moment tensor which describes a point seismic source (TRIFU and SHUMILA 2002). As such, evaluation of the event mechanism consists in the determination of the seismic moment tensor through the linear inversion of the above displacements. Worth noting, low frequency displacements can be calculated in the time domain, which allows for an automated estimate of source mechanisms (TRIFU *et al.* 2000). Before discussing the inversion results obtained for the recorded seismicity, the stability and reliability of the seismic moment tensor inversions are analyzed for the array geometry and sensor characteristics employed at Ocnele Mari (Fig. 2).

A measure of the stability of seismic moment tensor inversion is given by the Conditional Number (CN) (DUFUMIER and RIVERA 1997). This is defined as the ratio between the largest and smallest eigen values of the data matrix to be inverted (TRIFU *et al.* 2000). It is equal to one for a perfectly invertible matrix and approaches infinity for a very ill-conditioned matrix. CN can be interpreted as a data noise amplifier that defines the upper bound of the model parameter errors. Since it depends only on the source location and array geometry, expected CNs are calculated and displayed in Fig. 9a, b. Most stable

inversions (CN < 10) are expected for the sources located below 200 m elevation. In the close proximity to the major cavern ceiling the anticipated inversion CN is around 15 and increases towards the surface. In the immediate vicinity of most sensor wells CN reaches the highest values and these zones should be considered as 'blind spots' for inversions. Overall, the CN results suggest that reasonably stable moment tensor inversions are expected for the installed sensor array. Average CN estimates for actual inversions are calculated over the same grid and shown in Fig. 9c, d. In general, real CN values are in agreement with expected ones. Slightly higher levels of real estimates in some areas are easily explained by the extrapolation of observed CNs to no-data grid points.

To further analyze the stability and reliability of moment tensor inversions, data were randomly perturbed using a Monte-Carlo approach to simulate increased noise levels. Additionally, tests have been carried out to evaluate the effect of using three-component recordings, as compared with actual one-component recordings, from a potential array of sensors installed in identical locations. Figure 10 summarizes the results obtained for three arbitrarily chosen seismic events located in the vicinity of the major cavern ceiling. Based on actual event

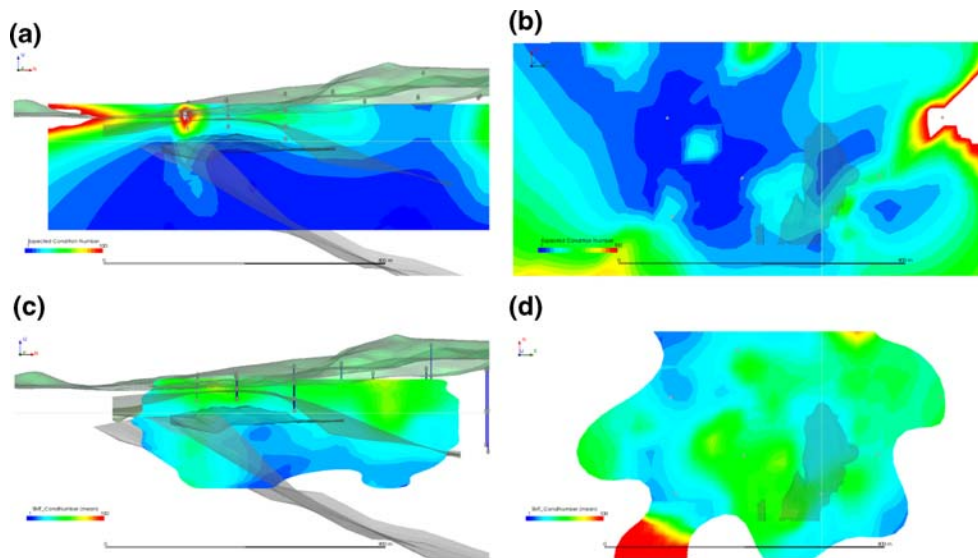


Figure 9

Expected (a, b) and average (c, d) condition number (CN, color scale from 1 to 100) in south-north vertical cross-section looking east and north-east plane at 200 m elevation looking down, respectively. *Horizontal* and *vertical thin light lines* show the positions of respective projections. Semi-transparent surface crossed by the *vertical line* in (b, d) is part of the major cavern that lies above 200 m elevation. *Scale bar* is 800 m

mechanism solutions, theoretical low frequency amplitude levels with first motion polarities were calculated for the P-, SV-, and SH-waves. These data were then perturbed by 10% Gaussian noise in the amplitude domain and random altering of 10% of first polarities.

For each particular moment tensor solution shown in column 1, 500 major double-couple (DC) solutions (JOST and HERRMANN 1989) obtained through random perturbations are displayed superimposed in columns 2 and 3 using a lower hemisphere equal angle projection (AKI and RICHARDS 1980). These results indicate that the use of one-component recordings provided by the geophone array installed at Ocnele Mari offers both stable and reliable seismic moment inversions. Interestingly, the use of three-component recordings would only lead to slightly more stable solutions. Automatic seismic moment tensor solutions have been obtained for 1,518 events. The distributions of Condition Numbers (CN) and multiple correlation coefficients (r^2) for this data set are shown in Fig. 11.

5. Analysis of Event Mechanisms

Due to previous massive collapses which occurred in 1991, 2001 and 2004, the salt deposit is expected

to contain highly fractured volumes with a heterogeneous local stress distribution. The collapsing of a fractured rockmass is compatible to the presence of both shear and non-shear fracture components. Consequently, it is anticipated that the seismicity generated by the controlled roof collapse will exhibit a large variety of seismic source mechanisms. After filtering out the events with $CN > 100$ and $r^2 < 0.5$, a data set of 912 solutions is available for further analysis.

Traditional 2D mapping of event mechanisms involves equal area or equal angle projections on the upper or lower hemisphere. This type of representation is adequate for tectonic seismicity with a relatively limited number of solutions and predominantly DC type mechanisms. In case of induced seismicity, however, source distribution is essentially 3D. To represent as much information as possible, each moment tensor solution will be shown as a 3D sphere with nodal planes defined by the major DC component.

A red-green-blue (RGB) 3D color space offers a convenient equivalent for the coloring of the tensional quadrants based on the fact that the absolute values of the decomposition coefficients into isotropic, compensated linear vector dipole (CLVD), and

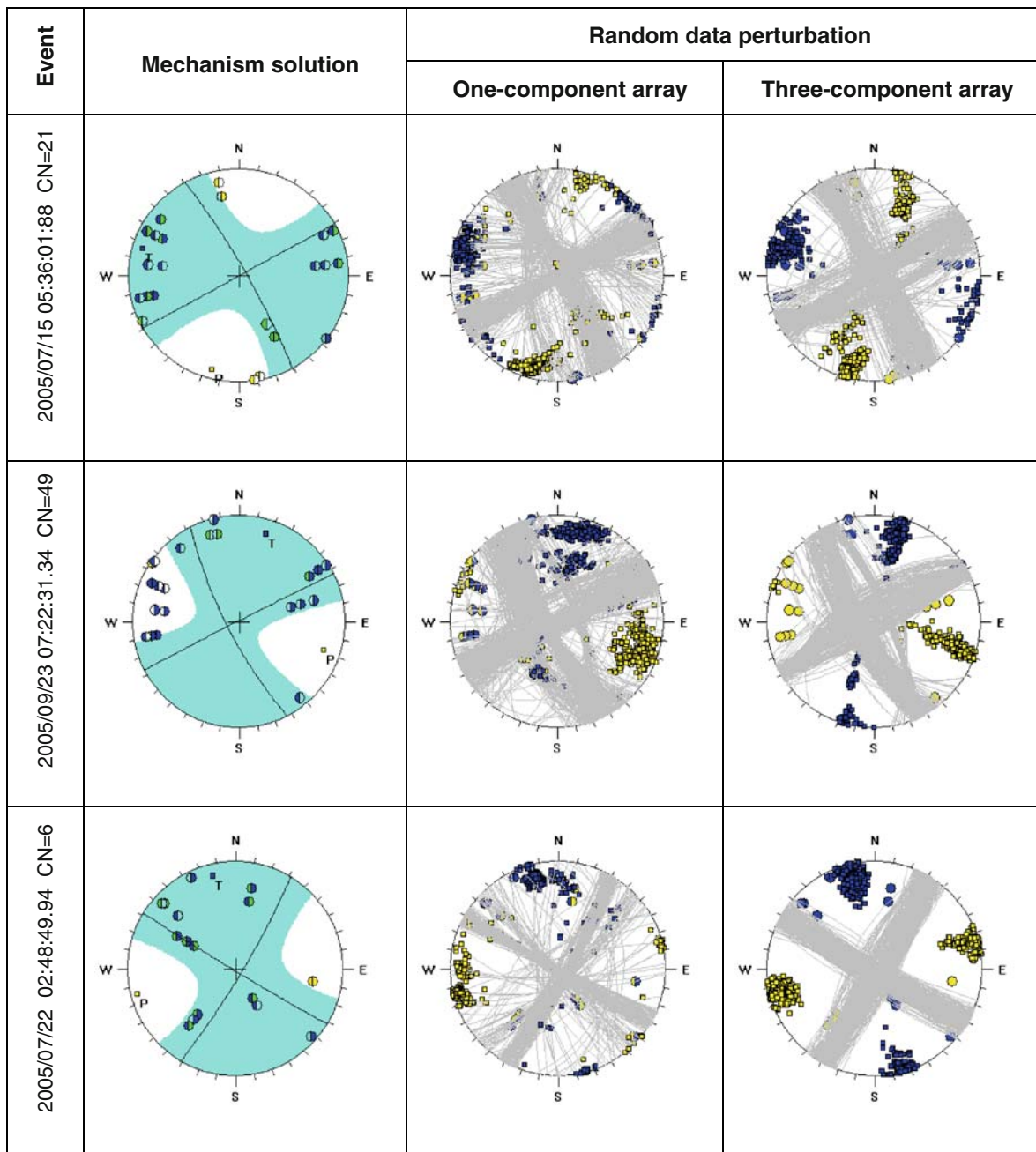


Figure 10

Stability of example moment tensor inversions (column 1) under 10% random perturbations for the one-component seismic array (column 2) and a hypothetical three-component array (column 3) at similar sensor locations

double-couple (DC) failure components vary between 0 and 1 and their sum is equal to one (VAVRYCUK 2001). Since present seismic monitoring arrays can provide online mechanism solutions for thousands of events, the visualization of this amount of

information is not trivial. Figure 12 shows the spatial distribution of the derived mechanism solutions. Its relationship with the underlying geological structures is apparent, particularly with the sinkholes caused by previous collapses.

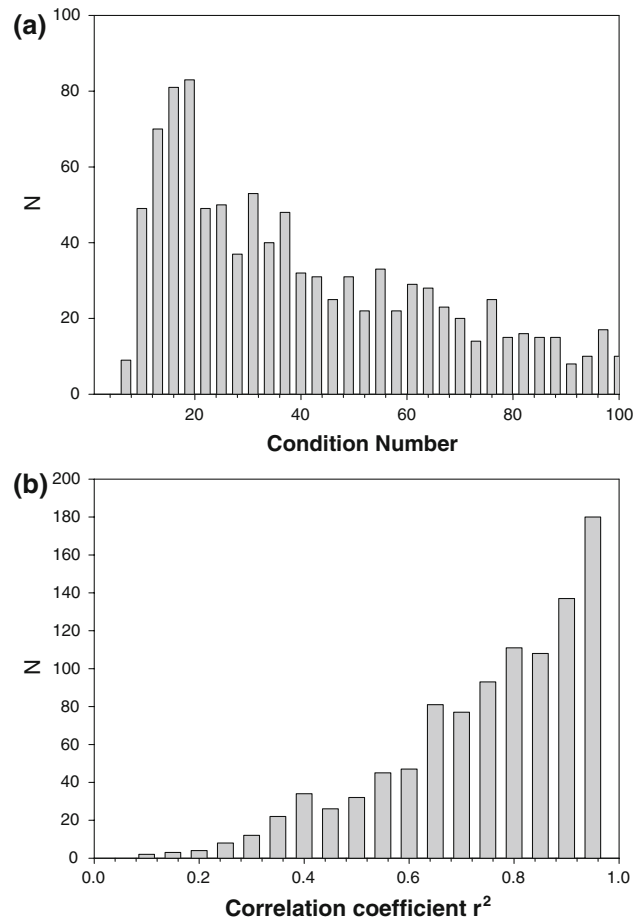


Figure 11

Condition number (a) and multiple correlation coefficient (b) distributions for automatic event mechanism solutions

Tension (T) and pressure (P) axes are presented in Fig. 12d for major DC components of the mechanism solutions. Spatial distribution exhibits the ‘broken glass’ pattern, a reflection of the local stress distribution in the highly fragmented upper part of the salt dome. Note the quasi-circular and radial orientation of the T and P axes, respectively, adjacent to the sinkhole.

A summary of the geometry of the shear faulting components and of mechanism distributions is presented in Fig. 13 on the faulting (FRÖHLICH 2001) and source type (HUDSON *et al.* 1989) diagrams. The faulting type diagram (Fig. 13a) shows that the data set predominantly contains normal and strike-slip events. The mechanism type diagram (Fig. 13b) also includes the location error ellipsoid in t – k coordinates, calculated using a linear error propagation

approach. Subvertical grid line (k) measures volumetric changes and remains constant along subhorizontal grid line (t) which characterizes departure from pure DC mechanism. Both coordinates range from -1 to $+1$. The following notations are used: \pm Crack for opening (+) or closing (–) tensile fault; \pm Dipole for force dipoles directed outward (+) or inward (–); \pm CLVD for compensated linear vector dipole with the sign determined by the direction of dominated dipole forces. As expected, the data-set reveals a variety of source mechanism types. Most events lay in the region containing the nodal planes of the P-wave radiation. This is the latitudinal strip between \pm Dipole marks. Also, note that majority solutions are in the area where tensile components of failure (slip vector out of faulting plane) are allowed.

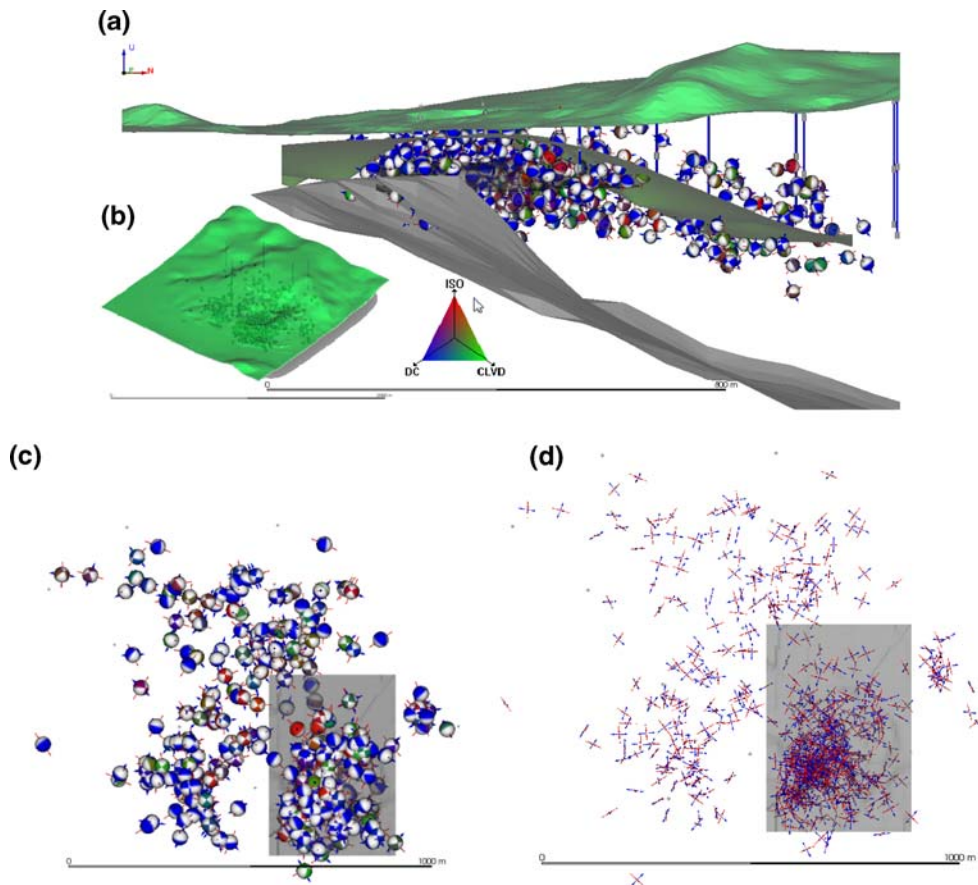


Figure 12

Event mechanism solutions in a cross-section looking east (a), with an aerial view of the monitoring area looking north-west (b), and in the northeast plan view looking down (c) with the dark rectangle showing the location of the cavern which collapsed in 2001. Distribution of T (blue) and P (red) axes (d). Scale bars are 800, 2,000, 1,000 and 1,000 m, respectively

Evaluating the failure components is important for the understanding of the stress re-distribution and geomechanical processes taking place on site. Although Fig. 13 provides an insight into seismicity generation in the area of the controlled collapse, it does not contain information on the spatial distribution of the failure components. To obtain this, the average parameter estimate is calculated over the closest events at each grid point by employing a nearest neighborhood approach with restriction on the search radius.

Spatial distribution of the isotropic failure component evaluated through the decomposition of the moment tensor solution is presented in Fig. 14a, b. Scale is from -10 to 100% . Negative and positive values indicate implosional (contraction) and explosive (expansion) volumetric changes, respectively. As expected for the geomechanical processes which

took place in the area under investigation, only a small part of the study volume was subjected to seismic events with implosional components of failure. It can be speculated that such events occurred either on the floor of the cavern under gravitational forces, or in places where the inter-chamber pillars were destroyed by dissolution processes. The results indicate that the vast majority of the mechanism solutions include up to 30% explosive failure components, which correspond to roof caving under gravitational collapsing.

DC components indicating pure-shear failure are shown in Fig. 14c, d. The largest such components correspond to events surrounding the cavern ceiling. Above and below this area the percentage of the DC component decreases. Note that low values that occur towards the map boundary are caused by very sparse sampling.

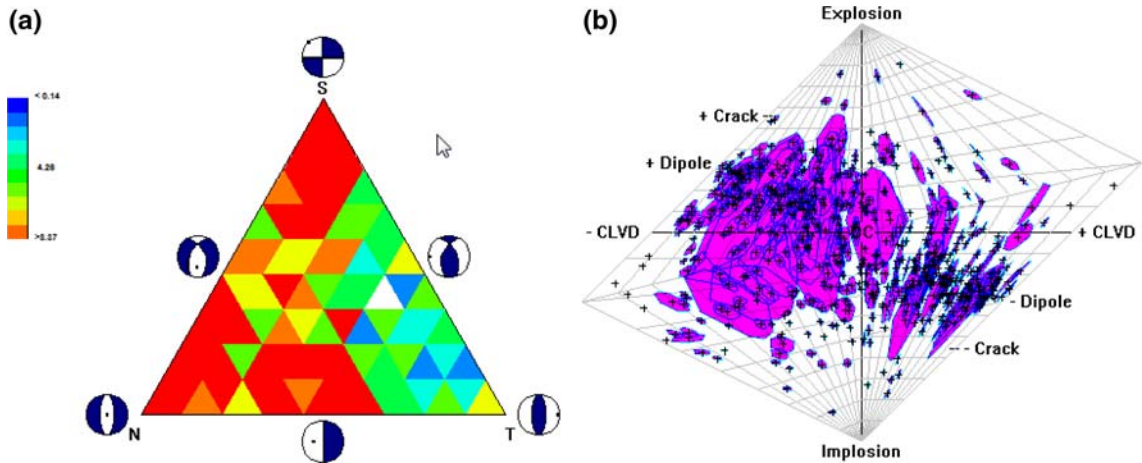


Figure 13
Faulting (a) and mechanism (b) type diagrams of the derived mechanism solutions

Distribution of the CLVD components is displayed in Fig. 14e, f. Such a failure component could correspond to a rotation of the plane of slip, or off-plane shear. Low percentage CLVD components dominate the mechanism solutions for the vast majority of the monitoring volume. The pronounced zones with a high percentage of CLVD are noted at the periphery of this volume and correspond to poor data sampling.

A generalization of the pure-shear point source model was proposed by VAVRYCUK (2001) in which the slip vector could be out of the faulting plane by an angle α called tensile angle. A positive angle indicates a tensional seismic source, whereas a negative value denotes a compressive source. Pure shear sources will have $\alpha = 0^\circ$, while 90° and -90° correspond to pure tensile and pure compressive sources, respectively. Tensile angle is estimated from the coefficients of the moment tensor decomposition and its spatial distribution is presented in Fig. 14g, h. Discarding extreme values at the boundary of the study volume, it is apparent that regions characterized by tensile/compressional values correlate well with pre-existing geological structures.

6. Seismic Deformation Field

When source locations are distributed over an entire volume rather than over a limited number of failure planes, the integrated seismicity can be treated

as a flow within the rock mass (RIZNICHENKO 1965). A formalization of this approach by KOSTROV and DAS (1988) shows that the integrated effect of N seismic sources that occurred in the elementary volume ΔV during the time interval Δt causes a deformation described by the following strain rate tensor

$$\dot{\epsilon}_{ik} = \frac{\sum_{n=1}^N M_{ik}^n}{2\mu\Delta V\Delta t} \quad (1)$$

where M_{ik}^n are the components of the second rank symmetric seismic moment tensor for the n -th event in ΔV , μ is the shear modulus, and i, k are indexes denoting the axes of the coordinate system. Standard approach for strain rate mapping was based on sparse regional seismicity, in which case it was necessary to account for missing small earthquakes. This was done by separating moment tensor geometry (failure components) and size (scalar seismic moment M_0). M_0 was then integrated using a recurrence law over the entire expected energy range in the volume of interest (KOSTROV and DAS 1988).

In the current study statistics are very rich. As such, there is no need to use a recurrence law for seismicity extrapolation. Instead, Eq. 1 can be applied directly. Evaluation of the strain rate tensor components is performed over a rectangular 3D grid with 20 m steps in both northing and easting coordinates, and 10 m step in elevation. At each grid point the volume comprising a predefined number of events is used as elementary volume ΔV . Time

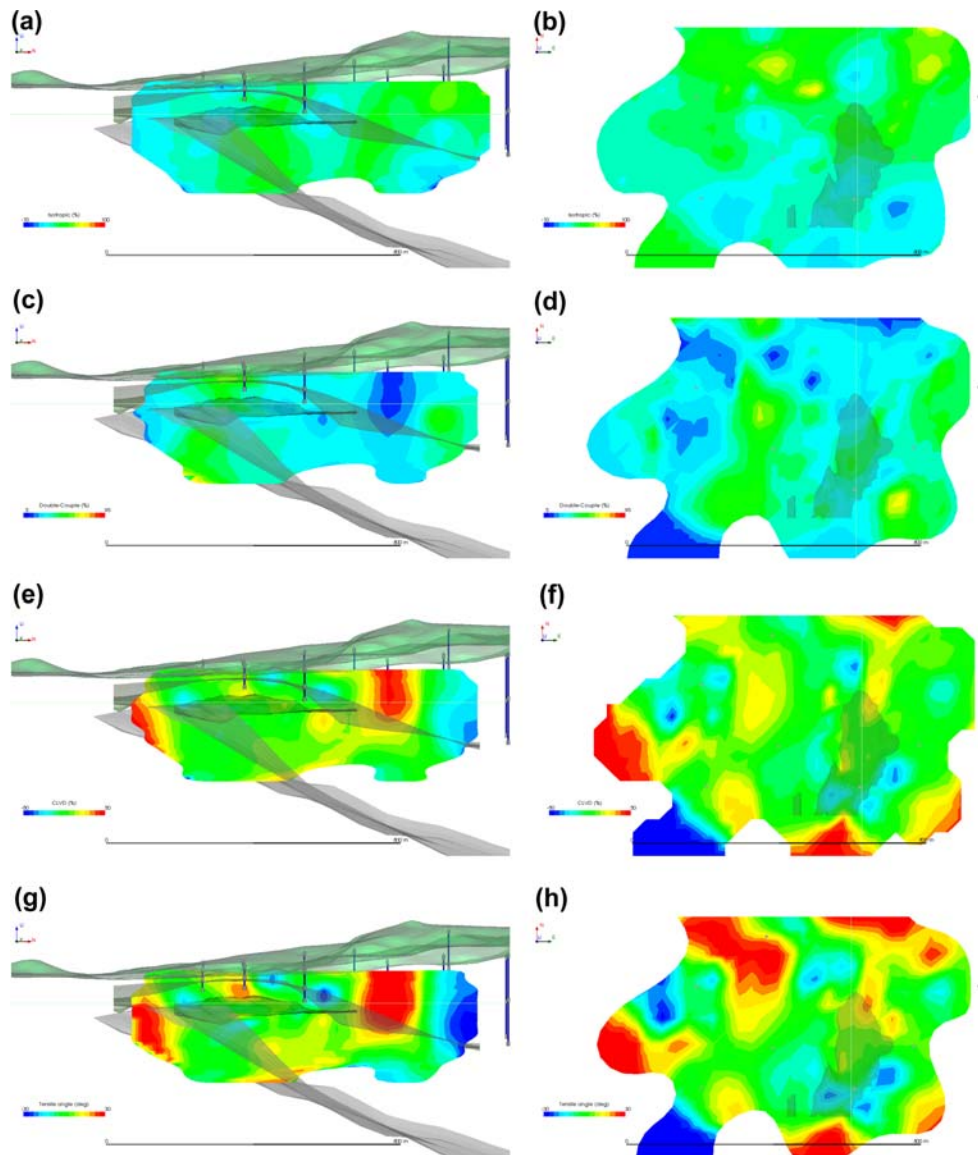


Figure 14

Isotropic—color scale from -10 to 100% (a, b), pure shear—from 5 to 95% (c, d), CLVD—from -50 to 50% (e, f) failure components and tensile angle—from -30 to 30% (g, h) in the south-north vertical cross-section looking east and the northeast plane at 200 m elevation looking down, respectively. The *horizontal* and *vertical thin light lines* show the positions of the respective projections. Scale bar is 800 m

interval between the first and last event occurrence in ΔV is considered as elementary time interval Δt in Eq. 1. Figures 15a, b display the vertical component of the strain rate tensor ($\dot{\epsilon}_{zz}$).

The highest vertical deformation rate tends to be related to pre-existing geological structures, such as the cavern roof and floor, as well as the rest of the salt formation. The horizontal component of the

strain rate tensor is defined as $\bar{u} = \{\dot{\epsilon}_{xx}, \dot{\epsilon}_{yy}\}$ and shown in Fig. 15c, d. The vector magnitude corresponds to the color code, while its direction is represented by the unit arrow. Note that the vertical cross-section is looking at the projection of unit direction. As expected, the horizontal deformation rate is most prominent in the areas of detected collapses.

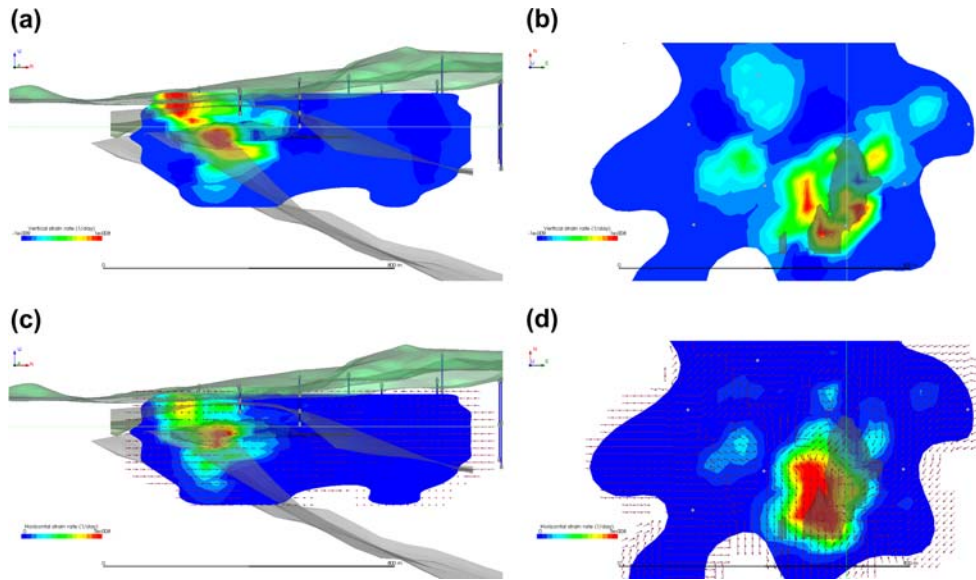


Figure 15

Vertical—color scale from -10^{-9} to 10^{-8} day^{-1} (a, b) and horizontal—from 0 to 5×10^{-8} day^{-1} (c, d) component of the strain rate in the south-north vertical cross-section looking east and the north-east plane at 200 m elevation looking down, respectively. Scale bar is 800 m

7. Conclusions

A deficient salt extraction program through solution mining has led over a period of 25 years to the formation at Ocnele Mari in Romania of a huge artificial underground cavern in Field II, containing many millions of cubic meters of brine. The cavern was located above and less than a kilometer away from the closest houses of a large community nearby. The presence of this amount of brine above a densely inhabited area created a considerable hazard for both personal property and human life. After the destruction of several individual houses through fast developing sinkholes, a major accident occurred in September 2001, followed by a second one in July 2004, accelerating the demand for a solution to this irreversible instability problem. A controlled collapse was proposed to cut open a ‘window’ in the roof of the underground cavern, pumping simultaneously the brine out and filling the cavern with sterile.

To evaluate the progress of the controlled collapse, microseismic monitoring was implemented within an area of over 1 km^2 . Twelve vertical boreholes were drilled from the surface to approximately 160–360 m deep. Three one-component 15 Hz omnidirectional geophones were installed in each

borehole. Data were recorded at 2 kHz sampling locally, at the top of each borehole, and continuously transmitted to a control center over radio Ethernet. In 9 months, from July 2005 to March 2006, 2,392 seismic events occurred with M_w -2.6 to 0.2 , which were located to an average accuracy of 18 m.

The linear decay of the cumulative frequency-magnitude distribution suggests a b -value of 1.5. It changes over time from 0.5 to 1 and then increases further to 1.5. The dimension D of the fracture process is often estimated as $D = 2b$. Thus, the controlled collapse was initiated as a linear fracture pattern. Three months later, once roof fragmentation was well developed, shear fractures dominated. Towards the end of the period reported in this study, fractures expanded throughout the entire monitored volume. The analysis of the ‘off-spring’ seismicity outlines a super-critical process. The relocation of seismicity through a collapsing technique allows the identification of various tight clusters. The most active clusters are closely associated with the main cavern collapse, whereas the less active clusters correspond to the roof fracturing of smaller size, nearby caverns.

Synthetic data with 10% random noise indicate that one-component geophone recordings allow for

stable and reliable event mechanism solutions through seismic moment tensor inversion of low frequency displacements calculated in the time domain, with first polarities attached. The use of three-component recordings at similar sensor locations would only marginally contribute to an increase in the stability and reliability of these solutions. A total of 1,518 event mechanisms have been derived for the seismicity which occurred from July and December 2005. Eliminating those characterized by a conditional number $CN > 100$ and a multiple correlation coefficient $r^2 < 0.5$, a data set of 912 solutions was retained for detailed analysis.

The analysis of spatial distribution of various failure components of the moment tensor solutions reveals interesting correlations with pre-existing geological and man-made structures on site. The tension (T) and pressure (P) axes for the major DC components exhibit a quasi-circular and radial orientation adjacent to the major sinkhole, respectively. The largest pure shear (DC) components characterize the events surrounding the cavern ceiling, which appear to exhibit normal and strike-slip failures.

The analysis of the isotropic failure component outlines that only a small part of the study volume was subjected to seismic events with implosional sources, associated with roof fragments striking the cavern floor under gravitational forces, or the dissolution of inter-chamber pillars. Worth noting, the majority of the mechanism solutions include up to 30% explosional failure components, which correspond to roof caving under gravitational collapsing. Low percentage CLVD failure components, perhaps indicative of shear occurring off the plane of slip, dominate the mechanism solutions within the monitoring volume. The presence of the CLVD and tensile faulting need further investigation. Meanwhile, the presence of high fluid pressure on site satisfies the main physical condition for permissible tensile faulting. Also, salt dissolution processes can produce failure components departing from pure shear.

Moment tensor solutions are further employed to evaluate the strain rate tensor components over a rectangular 3D grid with 20 m steps in both northing and easting coordinates, and a 10-m step in elevation. The highest vertical deformation rate relates closely to the cavern roof and floor, as well as the

rest of the salt formation, whereas the horizontal deformation rate is most prominent in areas of detected collapses.

The present study proves that automatic event mechanism evaluation reflects expected trends for controlled salt mine collapsing. Further studies should analyze the evolution of the mechanism solutions over time, since this has the potential to offer indicative elements for detecting the initiation of the above processes and thus contribute to the assessment of the progress and control of this engineering activity. Such an analysis will obviously benefit from information pertaining to the geotechnical measurements carried out on site during the controlled collapse, such as surface crack orientation and size, rate of water inflow, brine pressure, etc.

Acknowledgments

We acknowledge Ervin Medves (ERM SRL) and Florian Zamfirescu (Universitatea Bucuresti) for their efforts towards the implementation of the passive microseismic monitoring technology at Ocnele Mari. Alexandru Danchiv, Monica Andrei, Marius Mocuta (Universitatea Bucuresti), Valentin Filip, Marius Mateica (S.C. FlowTex Technology SA), Ian Leslie and Mike Smith (Engineering Seismology Group Inc.) are acknowledged for their sustained contribution to the maintenance of the microseismic system. Additionally, we would like to thank Florian Zamfirescu and Alexandru Danchiv for various discussions on technical aspects related to this project.

REFERENCES

- AKI, K. and RICHARDS, P.G., *Quantitative Seismology: Theory and Methods* (W.H. Freeman, San Francisco, 1980).
- DUFUMIER, H. and RIVERA, L. (1997), *On resolution of the isotropic component in moment tensor*, Geophys. J. Int. 131, 595–606.
- FROHLICH, C. (2001), *Display and quantitative assessment of distributions of earthquake focal mechanisms*, Geophys. J. Int. 144, 300–308.
- HELMSTETTER, A. and SORNETTE, D. (2002), *Sub-critical and super-critical regimes in epidemic models of earthquake aftershocks*, J. Geophys. Res. 107, 2237–2257.
- HUDSON, J.A., PEARCE, R.G., and ROGERS, R.M. (1989), *Source type plot for inversion of the moment tensor*, J. Geophys. Res. 94, 765–774.

- JONES, R.H. and STEWART, R.C. (1997). *A method for determining significant structures in a cloud of earthquakes*, J. Geophys. Res. *102*, 8245–8254.
- JOST, M.L., and HERRMANN, R.B. (1989). *A student's guide to and review of moment tensors*, Seism. Res. Lett. *60*, 37–57.
- KOSTROV, B.V. and DAS, S., *Principles of Earthquake Source Mechanics* (Cambridge University Press, Cambridge, UK, 1988).
- PRESS, W.H., FLANNERY, B.P., TEUKOLSKY, S.A., and VETTERLING, W.T., *Numerical Recipes: The Art of Scientific Computing (Fortran Version)* (Cambridge University Press, Cambridge UK, 1989).
- RIZNICHENKO, Y.V., *Seismic rock flow*, In *Dynamics of the Earth Crust*, Nauka, Moscow (in Russian), 1965.
- TRIFU, C-I., ANGUS, D., and SHUMILA, V. (2000). *A fast evaluation of the seismic moment tensor for induced seismicity*, Bull. Seismol. Soc. Am. *90*, 1521–1527.
- TRIFU, C-I. and SHUMILA, V. (2002), *The use of uniaxial recordings in moment tensor inversions for induced seismic sources*, Tectonophysics *356*, 171–180.
- TRIFU, C-I. and SHUMILA, V. (2005). *Seismic hazard assessment in mines using a marked spatio-temporal point process model*, In *Controlling Seismic Risk* (eds. POTVIN, Y., and HUDYMA, M.), Australian Centre for Geomechanics, Perth, Australia, pp. 461–467.
- VAVRYCUK, V. (2001), *Inversion for parameters of tensile earthquake*, J. Geophys. Res. *106*, 16339–16355.
- ZAMFIRESCU, F., MOCUTA, M., CONSTANTINESCU, T., NITA, C., and DANCHIV, A., *The main causes and processes of instability evolution at Field II of Ocnele Mari – Romania*, In *Proc. Solution Mining Research Institute Spring Meeting*, 28 April – 2 May, 2007a, Basel, Switzerland, 6 pp.
- ZAMFIRESCU, F., MOCUTA, M., DIMA, R., CONSTANTINESCU, T., and NITA, C., *A technical solution for the collapse fragmentation of the Field II cavern – Ocnele Mari, Romania*, In *Proc. Solution Mining Research Institute Spring Meeting*, 28 April – 2 May, 2007b, Basel, Switzerland, 8 pp.

(Received October 21, 2008, revised May 20, 2009, accepted May 22, 2009, Published online November 21, 2009)